

Multiphase CO₂ Dispersions in Microfluidics: Formation, Phases, and Mass Transfer

Tsai-Hsing Martin Ho, Dan Sameoto and Peichun Amy Tsai*

Department of Mechanical Engineering, University of Alberta, Edmonton, Alberta T6G 2G8, Canada

ARTICLE INFO

Keywords:

High-pressure microfluidics
Multiphase CO₂ flow
Mass transfer
Phase change
Carbon utilization and storage

ABSTRACT

The dissolution and microfluidic mass transfer of carbon dioxide in water at high-pressure conditions are crucial for a myriad of technological applications, including microreactors, extractions, and carbon capture, utilization, and sequestration (CCUS) processes. In this experimental work, we use a high-pressure microfluidic method to elucidate the mass transfer process of CO₂ in water at high pressure. An intriguing multiphase CO₂ flow and dispersions are observed when operating at the pressure-temperature (P - T) condition close to the CO₂ gas-liquid phase boundary ($P = 6.5$ MPa and $T = 23.5 \pm 0.5$ °C). We propose a series of strategies to unravel this complex multi-phase dynamics by calculating each phase's volume and mass change in a gas-liquid coexistent CO₂ dispersion, estimating the possible CO₂ concentration change in water, and comparing with the CO₂ solubility data. Finally, we quantify the CO₂ mass transfer by directly calculating the CO₂ dissolution rate in water and estimating the volumetric mass transfer coefficient ($k_L a$). The results show that the mass transfer may be influenced by the specific area (a), CO₂ concentration gradient in the water slug, and the traveling speed of a dispersion.

1. Introduction

The technologies of carbon capture, utilization, and sequestration (CCUS) are essential to reduce CO₂ emissions and consequently mitigate global warming issues (Orr et al., 2018; Zhang et al., 2020). CCUS integrates methods to gather and transport CO₂ from large emission sites, such as power plants and oil refineries (Wilberforce et al., 2019). The concentrated CO₂ can be utilized for enhanced oil recovery (EOR) (Al Adasani and Bai, 2011) and enhanced coalbed methane (Prabu and Mallick, 2015; Mukherjee and Misra, 2018) for energy fuel production while sequestering CO₂, and the further purified CO₂ can be used for chemical synthesis (Meunier et al., 2020; Branco et al., 2020). Alternatively, the captured CO₂ can be stored in various geological formations, such as in ocean (Adams and Caldeira, 2008; Aminu et al., 2017), in sub-seabeds (Carroll et al., 2014; Teng and Zhang, 2018), and in deep saline aquifers for a long time (Bachu, 2015).

The CO₂ mass transport behavior, therefore, plays a critical role in many CCUS processes, including the CO₂ absorption in the capture process (Abolhasani et al., 2014; Wilberforce et al., 2019) and the CO₂ dissolution in the pore fluids of sequestration sites. For example, in EOR engineering precise data of CO₂ dissolution in the pore-fluids helps estimate the required injection pressure to reach the minimum miscibility pressure for a better recovery efficiency (Al Adasani and Bai, 2011). The CO₂ dissolution and mass transfer processes affect the storage capacity of deep saline aquifers during the early injection stage (via structural and residual trapping of CO₂ in micropores) as well as the long-term solubility trapping and mineralization of CO₂ with the host, porous rock (Huppert and Neufeld, 2014; Bachu, 2015; Aminu et al.,

2017). Furthermore, understanding the CO₂ mass transport processes helps evaluate the sealing integrity and calculate the pressure build-up and CO₂ leakage (Singh, 2018), which are essential for mitigating potential environmental impacts (Carroll et al., 2014; Blackford et al., 2014).

The early experimental investigations for measuring the CO₂ dissolution rate and mass transfer include both in-situ field experiments (Brewer et al., 1999, 2002; Blackford et al., 2014; Sellami et al., 2015) and laboratory measurements using stirred vessels (Van't Riet, 1979) or bubble column reactors (Shah et al., 1982; Kantarci et al., 2005). However, the field experiments usually are time- and budget-consuming, and most of the previous laboratory experiments require large apparatuses to handle working fluids at high pressure safely (Teng and Yamasaki, 2000; Ogasawara et al., 2001; Maalej et al., 2001) and therefore more space, resources, and experimental time. Hence, it motivates us to explore alternatives for acquiring essential mass transfer data at elevated pressure more efficiently since the relevant experimental studies are crucial but rare currently.

Microfluidics has become an emerging and useful tool for fluid physics (Anna, 2016; Amstad et al., 2017) as well as energy and environmental technologies due to its time and economic efficiency (De Jong et al., 2006; Kjeang et al., 2009; Sinton, 2014; Lifton, 2016). A variety of microfluidic platforms have been utilized to investigate the mass transfer rate of gases (e.g., CO₂ (Yue et al., 2007; Sun and Cubaud, 2011; Abolhasani et al., 2012), air (Yue et al., 2009), and ozone (Ren et al., 2012)) in different solvents, the CO₂ take-up capacity of physical solvents for CO₂ capture applications (Sun and Cubaud, 2011; Lefortier et al., 2012; Abolhasani et al., 2012), and the influence of temperature (Turmarkin et al., 2011) and surfactants (Shim et al., 2014) on CO₂ solubility in water. Moreover, the development of high-pressure microfluidic devices in the last decade enables ex-

* Corresponding author

E-mail address: peichun.amy.tsai@ualberta.ca
ORCID(s): 0000-0002-3095-3991 (P.A. Tsai)

periments to operate in a broader pressure (P) and temperature (T) range up to $P = 45$ MPa and $T = 500$ °C (Marre et al., 2012). A few of microfluidic studies exploiting high- P platforms provide insights into the CO_2 behaviors in different carbon storage scenarios, including the invasion patterns of CO_2 displacing the pore fluid (Zhang et al., 2011; Morais et al., 2016), the applications in the enhanced oil recovery (EOR) (Nguyen et al., 2015; Sharbatian et al., 2018), the physical properties at the supercritical state (Pinho et al., 2015), fast screening the CO_2 phase state in different solvents (Pinho et al., 2014; Bao et al., 2016), and the CO_2 solubility in brine (Liu et al., 2012).

Microfluidic studies addressing the mass transfer rate of CO_2 in water/brine at high P - T conditions, especially for the liquid and supercritical CO_2 , are still limited (Sell et al., 2013; Yao et al., 2015, 2017; Qin et al., 2017, 2018). Sell et al. (Sell et al., 2013) reported a minor influence of pressure on the CO_2 diffusion coefficient as P increased from 0.1 to 5 Mpa. In contrast, the salinity significantly hinders CO_2 diffusion process in water, with a decrease in the diffusion coefficient by 60% with increasing salinity (from 0 to 5 M).

Yao et al. studied the pressure effects on the CO_2 mass transfer rate in water by measuring the liquid side volumetric mass transfer coefficient, $k_L a$, under elevated pressure from 0.1 to 3 M Pa. They found that $k_L a$ increased with the rising pressure and attributed this to the enlarged cross-sectional area of a CO_2 bubble at high pressure, which increases the CO_2 -water contact area and enhances CO_2 mass transfer (Yao et al., 2015). Interestingly, they did not observe a significant influence of pressure on the CO_2 absorption in the chemical solvent DEA (diethanolamine) from their later experiments. They attributed to the shrinking interfacial area due to the altering flow patterns and the channel geometry (Yao et al., 2017).

Qin et al. calculated the mass transfer coefficient (k_L) from the shrinkage of supercritical CO_2 at 8 MPa and 40 °C according to the 3-D morphology of an ideal Taylor bubble in a rectangular channel (Qin et al., 2017). Their results showed that k_L rose from 1.5×10^{-4} to 7.5×10^{-4} m/s as the water volume fraction increased from 0.28 to 0.9. Additionally, CO_2 droplets with a faster-moving speed had a high k_L due to the strong inner recirculation in the water slugs, enhancing the mixing of CO_2 and water (Qin et al., 2018).

In this work, we experimentally investigate the dissolution of liquid CO_2 in water at the injection pressure $P_{\text{inj}} = 6.5$ MPa and room temperature, $T = 23.5$ °C. To the best knowledge of ours, we observe intriguing and remarkable multiphase-coexisting CO_2 dispersions at high pressure, for the first time, generated by a two-phase CO_2 flow merging with water at the microfluidic T-junction (see Figure 1), while most similar microfluidic studies using two-phase flow have focused on the generation of monodisperse segmented flows and associated fluid dynamics and patterns (Zhu et al., 2016; Laborie et al., 2016; Eggersdorfer et al., 2018; Chakraborty et al., 2019; Salari et al., 2020; Fan et al., 2020). To analyze the complex dynamics of the multi-component CO_2 droplets, which involves phase change and dissolution pro-

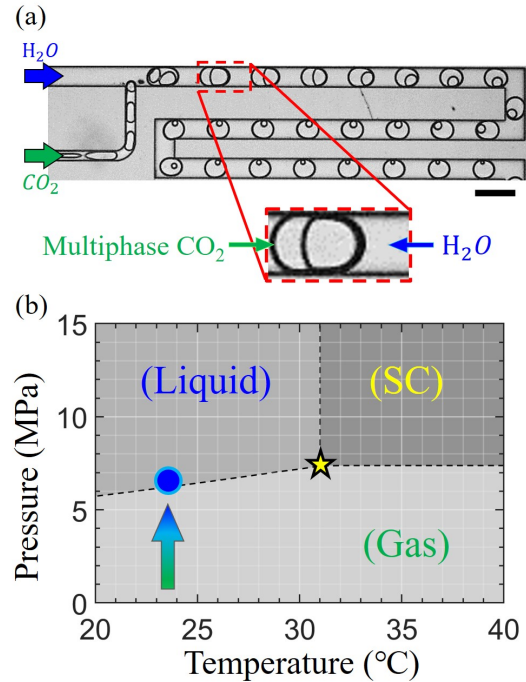


Figure 1: (a) An experimental snapshot of dispersions, containing multiphase (gas/liquid) CO_2 surrounded by the continuous phase of water, generated with a microfluidic T-junction. The scale bar represents $200 \mu\text{m}$. (b) Plotted in the CO_2 phase diagram are the experimental pressure and temperature conditions (shown by \bullet) where the coexisting multiphase dispersions are observed. Experimentally, the pressure of CO_2 was gradually increased to ≈ 6.5 MPa (\bullet) at room temperature, as the arrow indicates. The CO_2 saturation pressure at 23.5°C is 6.14 MPa, as the black dashed line shows the gas-liquid phase boundary of CO_2 . The phase diagram is plotted based on the database provided by the National Institute of Standards and Technology (NIST) (NIST, 2020).

cesses, we first differentiate the phase state of CO_2 inside the dispersion by comparing the mass change and the solubility limit in water (for a particular P and T condition). A detailed discussion is provided according to two different phase combinations. Based on these results, we further quantify the mass transfer process by calculating the dissolution rate of CO_2 , \dot{M}_{dis} , and calculating the volumetric mass transfer coefficient, $k_L a$. We find that the estimated $k_L a$ decreases rapidly with time, which may attribute to the change of the specific area, CO_2 concentration in the water slug, and the moving speed of dispersions.

2. Material and methods

We experimentally observed an intriguing two-phase CO_2 flow with a clear interface in the CO_2 injection channel before the microfluidic T-junction. Consequently, the multiphase coexisting CO_2 dispersions were formed in the T-junction microchannel after merging with Milli-Q water, as shown in Fig. 1a. The experiments were operated at the in-

jection pressure, $P_{inj} = 6.5 \pm 0.05$ MPa and the chip temperature, $T_{chip} = 23.5 \pm 0.5$ °C, as pointed by the blue circle (●) in Fig. 1b. The microchannel was fabricated using the deep reactive ion etching method (DRIE) (Franssila, 2010; Ho and Tsai, 2020). The main channel is 100 μm in width and 30 μm in height. The side-channel for introducing CO_2 is 50 μm in width and has the same height as the main channel.

2.1. Experimental

The microfluidics was installed in a metal platform that can sustain high-pressure. CO_2 pressure was ramped up from the atmospheric condition (0.1 MPa and 23.5 °C) to a high-pressure condition for transforming to the liquid state (6.5 MPa and 23.5 °C). This process was controlled by a high-pressure gas pump (ISCO 100DX), which directly connects with the gas tank (Praxair, RES K CO_2 99.998%). A back-pressure regulator (TESCOM BP 25 – 4000 PSI) was connected to the system's outlet to control the CO_2 flow rate by regulating a proper pressure gradient across the channel. Milli-Q water was loaded in stainless steel syringes and pumped by a syringe pump (Chemyx Inc. Fusion 6000) after one hour of degassing in a vacuum chamber. Water is injected at the flow rate of 10 $\mu\text{l}/\text{min}$ for the bubbly, intermittent, and annular-1 flow. The water injection rate for the annular-2 flow is lower, at 5 $\mu\text{l}/\text{min}$. A thermocouple (K-type) was attached to the microfluidic chip and to monitor the temperature. The flow was observed by using an inverted microscope (Zeiss Axio Observer 7 Materials, with a 5 \times objective) and recorded by a high-speed camera (Phantom V710L) at 5,000 frames per second (fps).

2.2. Image analysis

We applied a series of post-image processing functions in ImageJ (NIH Image) (Abràmoff et al., 2004) to measure the size of a single dispersion and track its position with respect to time. We first calibrated these data by comparing them with the manually measured results. The maximum difference between them is within 2.3 % in length. The measured data were further analyzed by using a customized code written in MATLAB (MathWorks ®). The variation between dispersions was evaluated by calculating the standard deviation of at least five bubbles for each representative flow pattern. The result showed good consistency in the size and position. The variance is about 2.5 % maximum in dispersion's length and within 2.9 % in displacement.

2.3. Estimations of the total volume and surface area of a CO_2 dispersion

From our experimental images we notice that a dispersion comprises a brighter area surrounded by the back contour, as shown in Fig. 2a. We consider this black contour line resulting from the curved CO_2 -water interface, which deflects the light and reduces the interface's brightness. The width of the black contour is measured to be about 8 μm . Therefore, we assume the geometry of a CO_2 dispersion is a planar disk, with two spherical caps on both ends (see

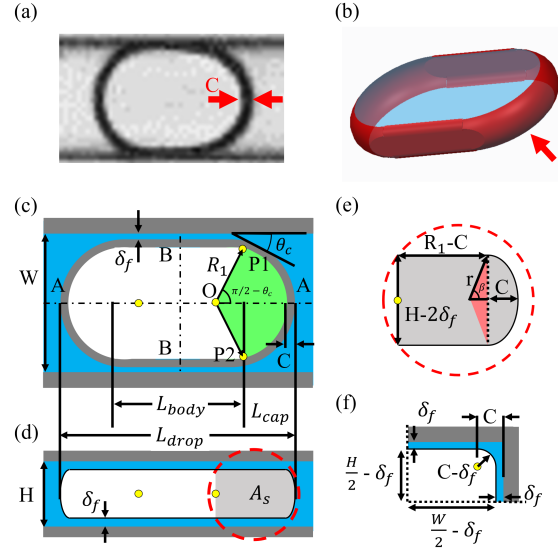


Figure 2: The schematic of an idealized microfluidic droplet, whose volume is comprised of a central section and two spherical caps on both ends. (a) Experimental snapshot of a CO_2 droplet. The black contour has a constant width, C (≈ 8 μm), for each droplet. (b) Schematic 3D model of CO_2 droplet volume. The red area is the curved CO_2 -water interface, resulting in the shadow area shown in (a). (c) The top view of a droplet with a total length of $L_{drop} = 2L_{cap} + L_{body}$. L_{cap} is the length of the circular caps, and L_{body} denotes the central section of a CO_2 droplet, which is assumed to have a liquid film of a constant thickness, δ_f , between the drop and sidewall. R_1 represents the radius of spherical caps that contact the sidewall with a contact angle, θ_c . C is estimated as the width of the dark area surrounding a droplet shown in (a). Both θ_c and C are measured from experiments. (d) The schematic drawing for the droplet's side-view. A_s denotes the cross-sectional area of the fan region (OP1P2) highlighted in color green in (c). (e) The detailed dimensions of the gray area A_s in (d). (f) The drawing of the quarter cross-section of the center body through the B-B plane.

Fig. 2b). The red area represents the curved CO_2 -water interface. Fig. 2c and 2d show the schematic shape of the CO_2 dispersion from the top view and the side view, respectively. The volume of a dispersion, V_T , is the sum of the center planar part and the two-sided caps:

$$V_T = 2V_{cap} + V_{body}. \quad (1)$$

The volume of the cap V_{cap} equals the volume of the green fan minus the volume of the triangle OPI2, from Fig. 2c. The volume of the green fan, V_{fan} , and triangle OP1P2, V_{tri} , can be written as:

$$V_{fan} = \frac{1}{2} \int_{-(\frac{\pi}{2}-\theta_c)}^{\frac{\pi}{2}-\theta_c} A_s R_1 d\theta, \quad (2)$$

$$V_{tri} = \frac{1}{2} (W - 2\delta_f) R_1 \cos\left(\frac{\pi}{2} - \theta_c\right) (H - 2\delta_f), \quad (3)$$

where W and H are the width and height of the channel, R_1 is the radius of the circular cap, θ_c represents the con-

tact angle between the (outer) cap and the microchannel (see Fig. 2c), and δ_f denotes the thickness of water film between CO₂ dispersion and the sidewall. A_s in Eqn. (2) is the cross-sectional area of the green fan through the A-A plane, as the gray area in Fig. 2d. The dimensions of A_s can be seen in Fig. 2e; note that the dimensions presented are exaggerated for better demonstration. A_s can be expressed as:

$$A_s = (R_1 - C)(H - 2\delta_f) + \beta r^2 - \frac{1}{2}r \cos \beta (H - 2\delta_f), \quad (4)$$

where r is the radius of the circular cap projected from the side view, and β is half of the central angle. We acquired these two parameters according to their geometrical relations:

$$r \cos \beta = r - C, \quad (5)$$

$$r \sin \beta = \frac{H}{2} - \delta_f. \quad (6)$$

The volume of the center body of a CO₂ dispersion is calculated as $V_{\text{body}} = A_c(L_{\text{drop}} - 2L_{\text{cap}})$, where $L_{\text{cap}} = R_1 \cos(\frac{\pi}{2} - \theta_c)$ is the length of the circular cap on both ends. A_c denotes the cross-sectional area of the center body through the B-B plane. We assume the center section's cross-sectional area is constant. Fig. 2f schematically demonstrates the idealized dimensions of this cross-section. We consider the shaded region of the body section is due to the curvilinear CO₂-water interface. A_c hence can be expressed as:

$$A_c = (W - 2\delta_f)(H - 2\delta_f) - (4 - \pi)(C - \delta_f)^2. \quad (7)$$

By substituting Eqn. (2), (3), and (7) into Eqn. (1), the volume of CO₂ dispersion is acquired. This calculation result agree well with the 3-D model built using computer-aided design software (PTC Creo), with an estimated, average error of 1.5%. Furthermore, a close examination of the CO₂ bubble/droplet shows a slightly asymmetric shape of 1 μm difference between the front and rear radii. We calculate the corresponding CO₂ bubble's volume using Eqn. (1) to Eqn. (7). The volume difference due to the asymmetric bubble geometry is about 0.4%.

3. Results and discussion

3.1. Multiphase CO₂ flow and dispersions

Fig. 3a–c are experimental snapshots, showing three distinct CO₂ multiphase flow patterns observed in the CO₂ channel before the T-junction (when $P_{\text{inj}} = 6.51$ and 6.48 MPa, $P_{\text{back}} = 6.15$ MPa and $T_{\text{chip}} \approx 23.5^\circ\text{C}$, close to the CO₂ gas–liquid phase boundary). The multiphase flow quickly transited from a segmented flow pattern (Fig. 3a) to a parallel flow with an upstream pinch-off nose, emitting segmented flow periodically (Fig. 3b). This parallel flow kept propagating along with the CO₂ channel and finally anchored at the T-junction, seen in (c). These three flow modes are similar to the classic condensation flows observed when flowing the vapor state of water (Wu and Cheng, 2005; Chen et al., 2014) or refrigerants (Coleman and Garimella, 2003;

Al-Zaidi et al., 2018) in the microchannel as the sidewall temperature (T_w) is lower than the vapor temperature of the fluid. We hence follow the same naming convention, calling the first segmented flow the "Bubbly flow" (Fig. 3a), the "Intermittent flow" for the second transitional pattern (in Fig. 3b), and the "Annular flow" for the final stratified flow pattern (in Fig. 3c). We artificially dyed the central or inner dispersed phase in light green in the images for better visualization.

At the microfluidic T-junction, the multiphase CO₂ flow periodically generates and emits dispersions in the main channel after being sheared off by the water flow. Fig. 3d shows such image sequences of the development of CO₂ dispersions for the different CO₂ flow patterns shown in Fig. 3a–c. These dispersions are multiphase with a clear interfacial boundary observed between the phases. Although each of the multi-phases is known to be either gas or liquid CO₂ because of the experimental pressure condition, without presumptions each exact phase was not certain and needed to be determined first. From the sequential images in Fig. 3 a–c, the inner phase (artificially dyed in light green) prefers to stay on the right side of a CO₂ dispersion, while the outer phase accumulates on the left. For clarification and convenience, we call the phase on the right side of the CO₂ dispersion the "inner (dyed) phase" and the other the "outer (undyed) phase" based on their appearance before the microfluidic T-junction (see Fig. 3 a–c).

Fig. 3e shows the total length of CO₂ dispersions, L_{drop} , changing with traveling time. The size change of the inner (dyed) phase seems to influence L_{drop} greatly. For dispersions generated by the bubbly flow (depicted by ●) and the intermittent flow (depicted by ■), L_{drop} decreases due to the shrinkage of the inner (dyed) phase. L_{drop} reaches the steady-state when the inner phase completely vanishes. In general, we observe the same behavior for most dispersions generated by the annular flow, as depicted by ◆ in Fig. 3d. However, we surprisingly observed a different size change behavior of inner (dyed) phase in some dispersions generated by the annular CO₂ flow. As shown in Fig. 3 (d4), the inner phase shrank at the beginning when the dispersion detached from the T-junction. However, it started to expand after the dispersion traveled around 60 ms in the main channel, leading to the growth of CO₂ dispersions after moving 55 mm away from the T-junction (depicted by ▲).

3.2. Determination of the phase states of a multiphase CO₂ dispersion

Before detailed analyses on CO₂ flow and dissolution dynamics, we have to first differentiate and analyze the exact phases in the multiphase CO₂ droplets/bubbles without any presumptions. Based on the experimental condition ($P_{\text{inj}} = 6.5$ MPa and $T_{\text{chip}} \approx 23.5^\circ\text{C}$), we knew the coexistence of liquid and gas CO₂ in a dispersion before the T-junction. However, it is challenging to identify the phase states from the experimental grayscale images directly. These phases' grayscale values were close, measured to be 133.7 (± 5.8) and 132.3 (± 6.3) for the inner (dyed) and outer (undyed)

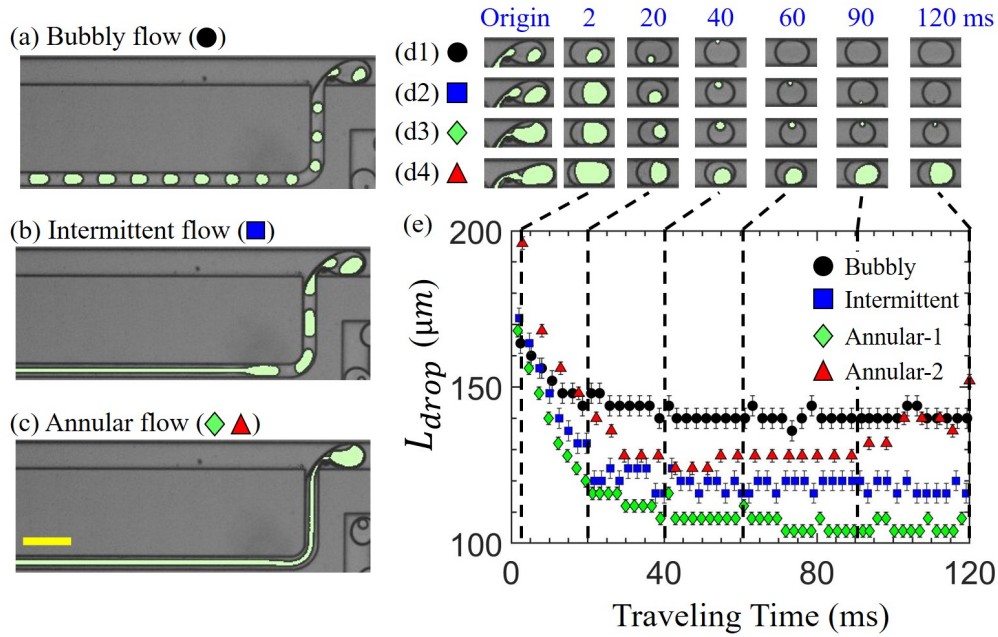


Figure 3: The snapshots of three different CO_2 flow patterns in our experiments: (a) the bubbly flow, (b) the intermittent flow, and (c) the annular flow. In the CO_2 channel, the inner part of CO_2 is highlighted in color light green. The yellow scale bar denotes $200 \mu\text{m}$. (d) Representative image sequences of gas-liquid coexisting CO_2 dispersions in water of the bubbly flow in (d1), the intermittent flow in (d2), and two annular flow cases in (d3)-(d4) (multimedia view). (e) the total length, L_{drop} , of dispersions changes with time in the main channel after the microfluidic T-junction. Notably, we observed two different phase change modes in the CO_2 annular flow pattern. The first one is named Annular-1 (depicted by \blacklozenge), and the second one is called Annular-2 (depicted by \blacktriangle), respectively.

phases, respectively. In addition, the surface tension at the water-gas CO_2 interface ($\sigma_{\text{W-G}} = 31.7 \text{ mN/m}$) is very close to that at the water-liquid CO_2 ($\sigma_{\text{W-L}} = 30.8 \text{ mN/m}$) (Pereira et al., 2016). This implies that both gas and liquid CO_2 could affix to the water and wrap the other phase. Here, we discuss the processes determining the phase state of CO_2 dispersions in more detail by analyzing the volume change, density difference, mass loss, and solubility in water.

Fig. 4a demonstrates the total volume of CO_2 dispersions, V_T , changing with time, while 4b and 4c show the volume fraction of the inner (dyed) phase (V_{in}) and of outer (undyed) phase (V_{out}), respectively. From the observations, V_{in} initially decreases dramatically for all representative cases, while V_{out} increases in the range of 25% – 30% of the change of V_{in} , implying the mass exchange between two phases inside a CO_2 dispersion. Dispersions with a larger initial V_{out} result in a bigger final size in the steady-state (flat regime), as seen in the bubbly flow (depicted by \bullet), comparing to other cases with larger V_{in} (depicted by \blacksquare , \blacklozenge , and \blacktriangle).

To systematically determine each exact phase (gas or liquid) for the multiphase CO_2 , we furthermore consider two different phase combinations and look into their corresponding mass change with time. By comparing with the CO_2 solubility data at 6.5 MPa and 23.5 $^\circ\text{C}$, this data would help differentiate the phase state in a CO_2 dispersion. The first presumption considers that the inner (dyed) phase is liquid CO_2 and the outer gas. The second presumption is the other

way, assuming that the inner (dyed) phase is gas and the outer liquid.

Fig. 5 shows the calculation results according to the two presumptions by showing the total cumulative mass, M_T , the net mass change, ΔM_T , and the estimated CO_2 concentration in water slugs, $|\Delta M_T|/V_{slug}$. Under the first presumption (assuming the inner (dyed) phase is liquid CO_2), M_T dramatically decreases in the first 20 ms and reaches the steady-state for dispersions of the bubbly, intermittent, and annular-1 flow, as shown in Fig. 5a. The net mass change, ΔM_T , during this period is between -5×10^{-11} to $-20 \times 10^{-11} \text{ kg}$, shown in Fig. 5b. Notably, dispersions in Annular-2 (\blacktriangle) show a gradual gain of the mass after 40 ms of traveling time, which is different from the previous three cases. Here, we consider that the mass transfer in a CO_2 dispersion includes two processes: (1) the phase transition between the two phases and (2) the dissolution of CO_2 into the surrounding water. The phase change processes should follow mass conservation, resulting in zero (or negligible) mass change (see Appendix A for a detailed analysis). Therefore, the net mass change, ΔM_T , should always be negative due to the dissolution.

We further estimate the CO_2 concentration in the water changing with time by dividing the absolute value of ΔM by the volume of the adjacent water slug, V_{slug} . Fig. 5c shows that the estimated CO_2 concentration for all repre-

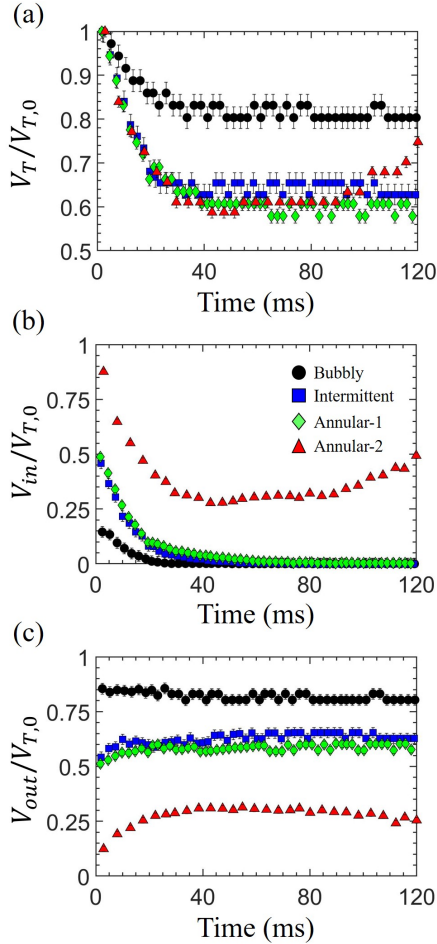


Figure 4: (a) The dimensionless volume of CO₂ dispersions changes with time, where V_T is estimated according to the method introduced in Section 2.3 using Eq.(1)-(7), and $V_{T,0}$ denotes the initial volume of a dispersion, i.e., $V_T(t=0)$. The corresponding fractional volume change of the inner (dyed) and outer phase inside the dispersion is presented in (b) and (c), respectively. dispersions generated by the three distinct CO₂ flow patterns are shown, including the bubbly flow (●), the intermittent flow (■), and the two different CO₂ phase change behavior observed in the annular flow [annular-1 (◆) and annular-2 (▲)].

sentative cases under presumption one is above 100 kg/m³, much higher than the CO₂ solubility in water, $S = 61$ (kg/m³), at the experimental conditions of $P_{inj} = 6.5$ MPa and $T_{chip} = 23.5$ °C (Diamond and Akinfiyev, 2003). Fig. 5d–f reveal the analyzed M_T , ΔM_T , and the estimated CO₂ concentration changing with time under the second presumption, respectively. The total cumulative mass of CO₂ dispersions decreases in a range of $1 \times 10^{-11} \sim 3 \times 10^{-11}$ kg, smaller than the results from the first presumption. All representative cases experienced an initial mass loss and reached steady-state at about 40 ms of traveling time. It should be noted that presumption two does not result in the strange mass gain in Annular-2 (depicted by ▲) in (d). Also, the net mass

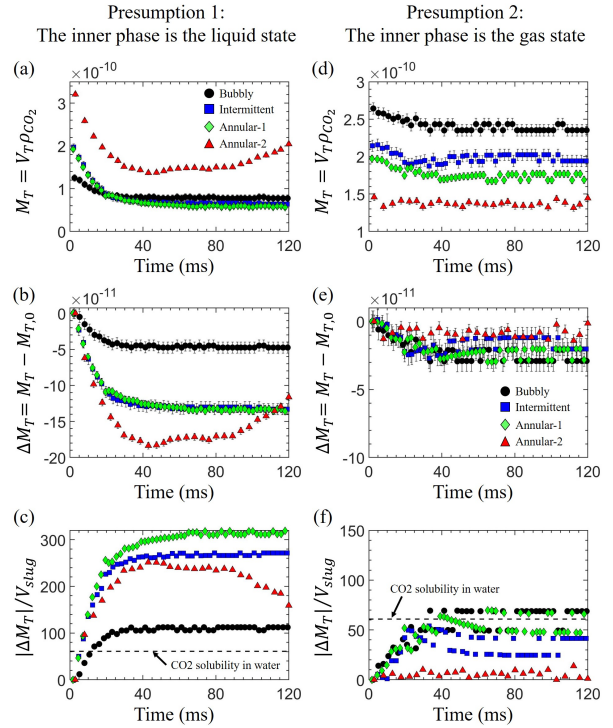


Figure 5: Results of time-varying CO₂ mass change estimated according to the presumption 1 and 2. (a) and (b) compare the cumulative mass of a CO₂ dispersion, $M_T = M_{in} + M_{out}$ (kg), changes with time, where M_{in} and M_{out} represent the mass of the inner (dyed) and outer phase of the dispersion, respectively. (c) and (d) show the net mass change of CO₂ dispersions, where $\Delta M_T = M_T - M_T(t=0)$ (kg). Here, the negative sign of ΔM_T implies the dissolution of CO₂ in the water. (e) and (f) demonstrate the CO₂ concentration change in water, estimated by dividing the absolute value of ΔM_T by the volume of adjacent water slug, V_{slug} (m³). The black dash line denotes the theoretical solubility of CO₂ in water at $P = 6.5$ MPa and $T = 23.5$ °C (Diamond and Akinfiyev, 2003).

loss, $\Delta M_T = M_T - M_T(t=0)$, is between -1×10^{-11} to -3×10^{-11} kg, giving the estimated CO₂ concentration in a range between 13.8 and 69.7 kg/m³. This range is consistent with the CO₂ solubility data in the literature, $S = 61$ (kg/m³) (Diamond and Akinfiyev, 2003).

The above analyses show that the second presumption yields consistent results with the CO₂ solubility data given P and T . Therefore, we confirm that the inner (dyed) phase is CO₂ gas state, and the outer phase is the liquid state. This conclusion is further validated due to the following two reasons. First, the volume change ratio of the outer to inner phase, V_{out}/V_{in} , is about 0.25–0.3. This value is also close to the density ratio of gas to liquid CO₂, $\rho_g/\rho_l = 0.33$, suggesting the shrinkage of the inner (dyed) phase in a CO₂ dispersion is the process combining the phase transition from the gas to liquid and the dissolution into the surrounding water. Second, presumption one yields an unusual increase in the total mass of case Annular-2 (demonstrated in Fig. 4a),

implying that this assumption is incorrect because there are no other external mass sources. Besides, the presumption one overestimates the amount of dissolving CO₂ in water.

3.3. Formation of multiphase CO₂ dispersions

We further look into how the multiphase flow is formed in the CO₂ channel and what happens to such a CO₂ dispersion evolving in the microchannel, as seen in Fig. 3. These multiphase patterns are observed when increasing P_{inj} from 1 atm up to 6.5 MPa at room temperature, and CO₂ in the pump started to phase change from the gas to liquid state slowly. Most of CO₂ likely stayed in the gas state as the oversaturated CO₂ vapor.

As CO₂ entered the microfluidics, CO₂ in the gas state flows in the center of the CO₂ channel, while the liquid CO₂ stayed on sidewalls because it is more viscous than the gas state. The formation of three distinct flow patterns observed might be similar to the jetting flow generated using the co-flow (Utada et al., 2007) and the cross-type microchannel (Cubaud and Mason, 2008). This kind of flow pattern may occur when the central fluid's velocity (gas CO₂) is greater than the outer one (liquid CO₂). The upstream annular flow may form because the inertia force from CO₂ gas stream stabilizes with the viscous force and surface tension at the gas-liquid interface (Utada et al., 2007). At the nose of the central CO₂ stream, gas bubbles detached and became the downstream bubbly flow, which might be triggered by the amplified capillary waves due to the surface tension gradient (Utada et al., 2008). The intermittent flow may be the transition between the bubbly and the annular flow. We observed that the intermittent flow emits droplets/bubbles downstream while upstream became an annular flow.

After the CO₂ flow merging with the continuous water phase, the multiphase CO₂ dispersions were formed periodically. The vapor CO₂ in a dispersion (i.e., the dyed inner phase) continued to transform from the gas to the liquid state, resulting in the rapid shrinkage of inner phase when moving in the main channel, as shown in Fig. 3d (first three rows). The expansion of dispersion in Annular-2 case (as demonstrated by ▲ in Fig. 3d and 3e) might due to the lower CO₂ vapor temperature than the microchannel's sidewall temperature. The local pressure along the channel keeps decreasing due to the hydraulic pressure gradient that drives the movement of a CO₂ dispersion (Kundu et al., 2011). CO₂ vapor temperature drops with the descending pressure, based on the Clausius-Clapeyron relation (Bejan, 2016), leading to the $P - T$ condition moving toward the phase boundary (Fig. 1b). Once the vapor temperature decreases to the sidewall temperature, CO₂ starts phase change from the liquid to gas state and expands L_{drop} .

3.4. Mass transfer of the multiphase CO₂ dispersions

To unravel the dissolution process while phase change is taking place, we develop an analysis to estimate the volumetric mass transfer coefficient, $k_L a$ (1/s), of CO₂ in water according to the dissolution rate of CO₂, \dot{M}_{dis} , and mass

conservation. We first assume that the continuous phase, water, is initially free from CO₂. Both gas and liquid CO₂ are incompressible due to the negligible density variation in a small pressure difference (estimated ~ 22 kPa). The CO₂ dissolution rate equals the net mass change rate of a dispersion, which can be expressed to the sum of the liquid and the gas parts:

$$\dot{M}_{dis} = \frac{dM_T}{dt} = \rho_l \frac{dV_l}{dt} + \rho_g \frac{dV_g}{dt}, \quad (8)$$

where ρ_l (ρ_g) is the density of CO₂ in the liquid (gas) state. V_l (V_g) denotes the volume of liquid (gas) CO₂. By integrating Eqn. (8), the total mass of dissolving CO₂ is expressed as:

$$\int_0^t \dot{M}_{dis} dt = \rho_l (V_l - V_{l,0}) + \rho_g (V_g - V_{g,0}), \quad (9)$$

where $V_{l,0}$ and $V_{g,0}$ (m³) denotes the volume of liquid and gas CO₂ at $t = 0$, respectively.

The dissolved CO₂ increases its concentration in a water slug, and the convective mass transfer can be expressed as: (Yao et al., 2015; Ho et al., 2021)

$$\dot{M}_{dis} = -k_L A_T (C^* - C(t)) = -V_{slug} \frac{dC}{dt}. \quad (10)$$

Here, k_L (m/s) denotes the mass transfer coefficient of CO₂ in water. A_T (m²) is the surface area of a dispersion, and V_{slug} is the volume of the adjacent water slug. C^* and $C(t)$ represent the saturation concentration of CO₂ in water and the mean CO₂ concentration in a water slug, respectively.

The CO₂ concentration change in the water slug, $C^* - C(t)$, can be written as an exponential function by integrating the second identity in Eqn. (10), so $C^* - C(t) = (C^* - C_0)e^{-k_L a t} = S e^{-k_L a t}$. The dissolved CO₂ in water as a function of time thus can be expressed as:

$$\dot{M}_{dis} = -k_L a S V_{slug} e^{-k_L a t}, \quad (11)$$

where C_0 is the initial CO₂ concentration in water. Because we assume water is initially free from CO₂, $C^* - C_0$ represents the CO₂ solubility in the water (S) in the unit of kg/m³. $a \equiv A_d/V_{slug}$; The volumetric mass transfer coefficient, $k_L a$, is associated with the mass change of CO₂ with time via integrating Eqn. (9) after substituting \dot{M}_{dis} by Eqn. (11):

$$k_L a = -\frac{1}{t} \ln \left\{ 1 + \frac{1}{S V_{slug}} [\rho_l (V_l(t) - V_{l,0}) + \rho_g (V_g(t) - V_{g,0})] \right\}. \quad (12)$$

It should be noted that Eqn. (10) and Eqn. (11) consider a flat CO₂-water interface for the mass transfer. Studies have shown that the Laplace pressure between the two phases can enhance gas molecules' transport of a stationary gas bubble into the surrounding solvent due to the overpressure. This enhancement becomes significant when the bubble radius is

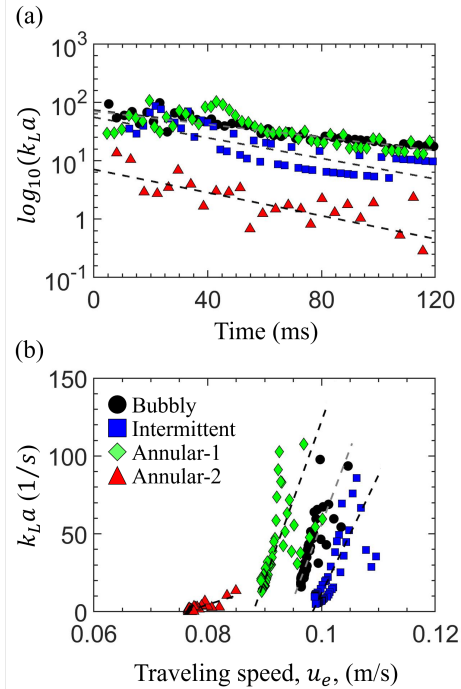


Figure 6: (a) The semi-log plot of estimated volumetric mass transfer coefficient, $k_L a$, of CO_2 changes with time. The black dashed lines are fitting curves showing the linear relation of $\log_{10}(k_L a)$ to time t . (b) The correlations of the estimated $k_L a$ and the traveling speed of CO_2 dispersions, u_e . The black dashed line represents the linear function of $k_L a = \alpha u_e + \beta$. Here, u_e is defined by dividing the displacement from the origin by the traveling time.

smaller than $15 \mu\text{m}$ and the solvent is nearly saturated (Kloek et al., 2001; Duncan and Needham, 2004). In our experiments, we degas water for an hour to ensure it is initially free from any dissolving gases, including CO_2 . A large concentration difference between CO_2 dispersion and adjacent water would primarily drive the mass transfer of CO_2 (Duncan and Needham, 2004). In addition, the Laplace pressure at $P_{\text{inj}} = 6.5 \text{ MPa}$ is estimated to be 1.5 kPa (about 0.023% of P_{inj}). Therefore, the influence of the Laplace pressure or surface curvature on the CO_2 mass transfer is likely negligible in our cases.

Fig. 6a shows the semi-log plot of the estimated $k_L a$ for four representative cases by using Eqn. (12). All cases show a decreasing trend of $\log(k_L a)$ with a slope of -7.5 ± 2.2 . The black dashed line depicts the linear function as an eye guide. Overall, the average $k_L a$ is estimated to be 25 (1/s) , which is consistent with our previous experimental results from injection pressures smaller than 8.5 MPa , giving the value of 29 (1/s) on average (Ho et al., 2021). This dynamic change in $k_L a$ was also observed and reported in a recent sub-millimeter scale experimental study of CO_2 mass transfer in water (Zhang et al., 2018).

The decreasing trend of $k_L a$ may attribute to the three following factors. First, the specific area (a) decreases with the reducing length of CO_2 dispersion L_{drop} due to phase

change and dissolution, where a is defined by the ratio of the surface area of a CO_2 dispersion (A_T) and the sum of V_T and V_{slug} . Second, the CO_2 concentration across the water- CO_2 interface is initially high as water contacts with CO_2 at $t \approx 0$, leading to the large $k_L a$ because CO_2 molecules dissolve in water in a very short time. The dissolution rate of CO_2 would quickly drop due to the surrounding water gradually saturated with CO_2 . Finally, we found that the traveling speed of CO_2 , u_e , influences $k_L a$ significantly.

Fig. 6b shows that $k_L a$ is the linear function of $\alpha \cdot u_e + \beta$ for all representative cases. The fitting coefficient α shows a larger value of $9150.9 (\pm 1383.9)$ for the bubbly (●), intermittent (■), and annular-1 (◆) cases. A smaller α of 1162.9 is found for the annular-2 (▲). The faster u_e allows fluid elements to pass the body part of CO_2 dispersions in a shorter time, preventing the fluid element from saturated with CO_2 and therefore increasing the mass transfer rate. Also, a high u_e induces more intensive inner circulation inside the water slug, enhancing the mixing of dissolving CO_2 in the water (Günther et al., 2005; Kuhn and Jensen, 2012).

Furthermore, the annular-2 flow shows a smaller estimated $k_L a$ than the other three flow patterns. The data suggest that the pattern of the multiphase CO_2 flow and the water injection rate play a significant role in CO_2 mass transfer. The annular-2 flow is observed at the water injection rate of $5 \mu\text{l/min}$, whereas the other cases are generated at a high water injection rate of $10 \mu\text{l/min}$. The small water injection implies the weaker shear stress exerting from the continuous water on the dispersed CO_2 phase. As a result, the water phase takes a longer time to rupture the multiphase CO_2 stream and thus generates longer CO_2 dispersions ($177.2 \pm 2 \mu\text{m}$) and water slugs ($216.8 \pm 1.6 \mu\text{m}$). The average length of CO_2 dispersions and water slugs for the bubbly, the intermittent, and the annular-1 flows are $162.9 \pm 4 \mu\text{m}$ and $109.1 \pm 4 \mu\text{m}$, respectively. The long CO_2 dispersion may prohibit the CO_2 mass transfer due to the inactive liquid film surrounding the CO_2 dispersion (Irandoust et al., 1992; Pohorecki, 2007). In addition, a long water slug may also hinder the mass transfer of CO_2 to water due to the inefficient mixing inside the water slug (Bercic and Pintar, 1997; Yao et al., 2021). As a result, the annular-2 flow shows a small $k_L a$ than the other cases.

4. Conclusions

We experimentally investigate an intriguing dissolving dynamics of multiphase CO_2 dispersions in water at the P-T condition close to the gas-liquid phase boundary of CO_2 ($P = 6.5 \text{ MPa}$ and $T = 23.5 \pm 0.5 \text{ }^\circ\text{C}$). The multiphase CO_2 dispersions are generated by merging the gas-liquid CO_2 flow with water using a microfluidic T-junction. Three flow patterns were observed sequentially, from the bubbly flow to the intermittent flow and the annular flow, representing the gaining dominance of the central CO_2 vapor stream over the liquid. A series of strategies are proposed and discussed to differentiate the phase state of CO_2 inside a dispersion, including estimating the volume of two distinct phases, calculating the corresponding mass change, and evaluating the

possible CO₂ concentration change in the water. We find that the gas CO₂ with lower viscosity traveling faster at the center of the CO₂ channel and could be pitched off to form bubbles surrounded by liquid CO₂.

We further estimate the volumetric mass transfer coefficient, $k_L a$, from the multiphase dispersion dissolving into the surrounding water by considering both dissolution and the phase change processes. The estimated $k_L a$ in our experiments ($\approx 25 \text{ s}^{-1}$) is greater than those from previous experimental data (of $0.3 < k_L a < 1.6 \text{ s}^{-1}$) obtained when P between 0.1 and 3 MPa (Yue et al., 2007, 2009; Ren et al., 2012; Yao et al., 2015). The larger $K_L a$ value found is likely attribute to the smaller hydraulic diameter used in our design ($d_c \approx 50 \mu\text{m}$), giving rise to a larger specific area (a) compared to previous work. Finally, the resultant $k_L a$ of the multiphase CO₂ dispersion shows an exponential decay with time due to decreasing a and, moreover, a significantly linear increase with the CO₂ traveling speed, u_e .

Conflict of Interest

There are no conflicts to declare.

Acknowledgments

We gratefully acknowledge the support from Canada First Research Excellence Fund (CFREF), Future Energy System (FES T02-P05) at the University of Alberta, and Canada Foundation for Innovation (CFI). We also thank S. Bozic and S. Munro for their help with micro-fabrications at the nanoFAB in the University of Alberta. P.A.T holds a Canada Research Chair in Fluids and Interfaces and gratefully acknowledges funding from the Natural Sciences and Engineering Research Council of Canada (NSERC) and Alberta Innovates (AI). This research was undertaken, in part, thanks to funding from the Canada Research Chairs Program.

Appendix

A. Detailed calculations of mass change of each phase due to phase change and dissolution

This appendix shows the case bubbly flow's detailed mass change calculations for supporting the discussions regarding Fig. 5. Each representative case demonstrated in Fig. 5 has gone through this type of analysis for determining the phase state of a CO₂ dispersion. For a CO₂ dispersion flowing in the microchannel, the total volume and mass is the sum of the inner (dyed) and outer phase, as seen in Fig. 7a–c. Fig. 7b and 7c demonstrate the mass of a CO₂ dispersion varying with time based on the two different phase combinations, using presumption 1 and 2.

The total CO₂ volume and mass can be estimated from the contributions of the inner (dyed) and outer phases:

$$V_T(t) = V_{in}(t) + V_{out}(t), \quad (13)$$

$$M_T(t) = \rho_{\text{CO}_2} V_{in}(t) + \rho_{\text{CO}_2} V_{out}(t). \quad (14)$$

The mass change of each phase comes from two primary parts: due to the phase change and the dissolution in water

(denoted by the subscript P and D , respectively):

$$M_{out}(t) - M_{out}(t_0) = m_{out}^D + m_{out}^P, \quad (15)$$

$$M_{in}(t) - M_{in}(t_0) = m_{in}^D + m_{in}^P, \quad (16)$$

where M_{out} (M_{in}) denotes the mass of the outer (dyed inner) phase. m^P represents the mass change due to the phase transition between the outer and inner phases; m^D is the mass loss due to its dissolution in water.

We consider the mass conservation during a phase change process and assume $m_{in}^P = -m_{out}^P$. The mass change of a CO₂ dispersion can be obtained by adding Eqn. (15) and Eqn. (16):

$$\Delta M_T(t) = M_T(t) - M_T(t_0) = m_{out}^D + m_{in}^D. \quad (17)$$

Fig. 7e–f present the results of $\Delta M_T(t)$ according to the two presumptions. Eqn. (17) implies that the mass of a CO₂ dispersion is always decreasing because CO₂ dissolves in water. Fig. 7d shows the estimated CO₂ concentration in the adjacent water slug, $C(t)$, compared with the theoretical CO₂ solubility in the water (black dashed-line). $C(t)$ was calculated by dividing the absolute value of ΔM_T in (e) and (f) by the volume of adjacent water slug, V_{slug} .

We can further estimate m_{in}^P by subtracting Eqn. (16) from Eqn. (15):

$$m_{out}^D - m_{in}^D + 2m_{in}^P = \Delta M_{in}(t) - \Delta M_{out}(t). \quad (18)$$

Here, we assume the dissolved CO₂ from both phases is comparable. Thus, the term $m_{out}^D - m_{in}^D$ is negligible compared to the $2m_{in}^P$ term. m_{in}^P can be expressed as half of the difference of $\Delta M_{in}(t)$ and $\Delta M_{out}(t)$:

$$m_{in}^P = \frac{1}{2} [\Delta M_{in}(t) - \Delta M_{out}(t)]. \quad (19)$$

The results calculated from Eqn. (19) are shown in Fig. 7g.

References

- Abolhasani, M., Günther, A., Kumacheva, E., 2014. Microfluidic studies of carbon dioxide. *Angew. Chem. Int. Ed.* 53, 7992–8002.
- Abolhasani, M., Singh, M., Kumacheva, E., Günther, A., 2012. Automated microfluidic platform for studies of carbon dioxide dissolution and solubility in physical solvents. *Lab Chip* 12, 1611–1618.
- Abràmoff, M.D., Magalhães, P.J., Ram, S.J., 2004. Image processing with ImageJ. *Biophotonics int.* 11, 36–42.
- Adams, E.E., Caldeira, K., 2008. Ocean storage of CO₂. *Elements* 4, 319–324.
- Al Adasani, A., Bai, B., 2011. Analysis of EOR projects and updated screening criteria. *J. Pet. Sci. Eng.* 79, 10–24.
- Al-Zaidi, A.H., Mahmoud, M.M., Karayiannis, T.G., 2018. Condensation flow patterns and heat transfer in horizontal microchannels. *Exp. Therm Fluid Sci.* 90, 153–173.
- Aminu, M.D., Nabavi, S.A., Rochelle, C.A., Manovic, V., 2017. A review of developments in carbon dioxide storage. *Appl. Energy* 208, 1389–1419.
- Amstad, E., Chen, X., Eggersdorfer, M., Cohen, N., Kodger, T.E., Ren, C.L., Weitz, D.A., 2017. Parallelization of microfluidic flow-focusing devices. *Phys. Rev. E* 95, 043105.
- Anna, S.L., 2016. Droplets and bubbles in microfluidic devices. *Annu. Rev. Fluid Mech.* 48, 285–309.

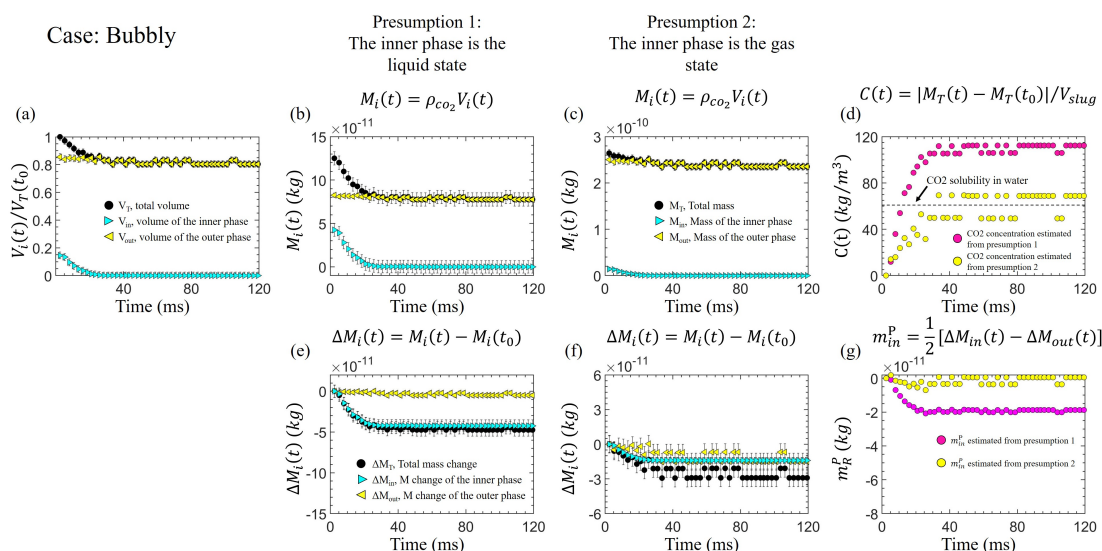


Figure 7: The detailed calculations of a CO₂ dispersion based on the mean value from five dispersions in the case of the bubbly flow. (a) The volume fractions, $V_i(t)$, of the outer phase (V_{out}), the (dyed) inner phase (V_{in}), and the total volume ($V_T = V_{out} + V_{in}$) changing with time (t). (b) The mass of the outer phase, $M_{out} = \rho_{CO_2} V_{out}$, and the dyed, inner phase, $M_{in} = \rho_{CO_2} V_{in}$, changing with time based on Presumption 1 (assuming the inner phase is the liquid CO₂). The total mass of a CO₂ dispersion, $M_T = M_{out} + M_{in}$. (c) Results of M_{out} , M_{in} , and M_T calculated from Presumption 2 (assuming the outer phase is the liquid CO₂). (e) and (f) present the net mass change of a dispersion varying with time calculated according to presumption 1 and 2, respectively. ΔM represents the variation of mass from its initial value, $M(t_0)$. The data for the outer phase is denoted by \blacktriangleleft , while the dyed inner phase by \blacktriangleright ; \bullet represents the sum properties. (d) The estimated CO₂ concentration, $C(t)$, changes with time according to presumption 1 (\bullet) and 2 (\circ). The black dashed line denotes the theoretical CO₂ solubility in the water. (g) The estimated mass change of the dyed, inner phase resulted from the phase transition.

- Bachu, S., 2015. Review of CO₂ storage efficiency in deep saline aquifers. *Int. J. Greenhouse Gas Control* 40, 188–202.
- Bao, B., Riordon, J., Xu, Y., Li, H., Sinton, D., 2016. Direct measurement of the fluid phase diagram. *Anal. Chem.* 88, 6986–6989.
- Bejan, A., 2016. *Advanced Engineering Thermodynamics*. John Wiley & Sons.
- Bercic, G., Pintar, A., 1997. The role of gas bubbles and liquid slug lengths on mass transport in the Taylor flow through capillaries. *Chem. Eng. Sci.* 52, 3709–3719.
- Blackford, J., Stahl, H., Bull, J.M., Bergès, B.J., Cevatoglu, M., Lichtschlag, A., Connelly, D., James, R.H., Kita, J., Long, D., et al., 2014. Detection and impacts of leakage from sub-seafloor deep geological carbon dioxide storage. *Nat. Clim. Change* 4, 1011–1016.
- Branco, J.B., Brito, P.E., Ferreira, A.C., 2020. Methanation of CO₂ over nickel-lanthanide bimetallic oxides supported on silica. *Chem. Eng. J.* 380, 122465.
- Brewer, P.G., Friederich, G., Peltzer, E.T., Orr, F.M., 1999. Direct experiments on the ocean disposal of fossil fuel CO₂. *Science* 284, 943–945.
- Brewer, P.G., Peltzer, E.T., Friederich, G., Rehder, G., 2002. Experimental determination of the fate of rising CO₂ droplets in seawater. *Environ. Sci. Technol.* 36, 5441–5446.
- Carroll, A., Przeslawski, R., Radke, L., Black, J., Picard, K., Moreau, J., Haese, R., Nichol, S., 2014. Environmental considerations for subsurface geological storage of CO₂: A review. *Cont. Shelf Res.* 83, 116–128.
- Chakraborty, I., Ricouvier, J., Yazhgur, P., Tabeling, P., Leshansky, A., 2019. Droplet generation at hele-shaw microfluidic T-junction. *Phys. Fluids* 31, 022010.
- Chen, Y., Shen, C., Shi, M., Peterson, G.P., 2014. Visualization study of flow condensation in hydrophobic microchannels. *AIChE J.* 60, 1182–1192.
- Coleman, J.W., Garimella, S., 2003. Two-phase flow regimes in round, square and rectangular tubes during condensation of refrigerant R134a. *Int. J. Refrig.* 26, 117–128.
- Cubaud, T., Mason, T.G., 2008. Capillary threads and viscous droplets in square microchannels. *Phys. Fluids* 20, 053302.
- De Jong, J., Lammertink, R.G., Wessling, M., 2006. Membranes and microfluidics: a review. *Lab Chip* 6, 1125–1139.
- Diamond, L.W., Akinfiev, N.N., 2003. Solubility of CO₂ in water from -1.5 to 100 °C and from 0.1 to 100 MPa: evaluation of literature data and thermodynamic modelling. *Fluid Phase Equilib.* 208, 265–290.
- Duncan, P.B., Needham, D., 2004. Test of the Epstein-plesset model for gas microparticle dissolution in aqueous media: effect of surface tension and gas undersaturation in solution. *Langmuir* 20, 2567–2578.
- Eggersdorfer, M.L., Seybold, H., Ofner, A., Weitz, D.A., Studart, A.R., 2018. Wetting controls of droplet formation in step emulsification. *PNAS* 115, 9479–9484.
- Fan, W.Y., Li, S.C., Li, L.X., Zhang, X., Du, M.Q., Yin, X.H., 2020. Hydrodynamics of gas/shear-thinning liquid two-phase flow in a co-flow mini-channel: Flow pattern and bubble length. *Phys. Fluids* 32, 092004.
- Franssila, S., 2010. *Introduction to Microfabrication*. John Wiley & Sons.
- Günther, A., Jhunjunwala, M., Thalmann, M., Schmidt, M.A., Jensen, K.F., 2005. Micromixing of miscible liquids in segmented gas-liquid flow. *Langmuir* 21, 1547–1555.
- Ho, T.H.M., Tsai, P.A., 2020. Microfluidic salt precipitation: implications for geological CO₂ storage. *Lab Chip* 20, 3806–3814.
- Ho, T.H.M., Yang, J., Tsai, P.A., 2021. Microfluidic mass transfer of CO₂ at different phases. unpublished data.
- Huppert, H.E., Neufeld, J.A., 2014. The fluid mechanics of carbon dioxide sequestration. *Annu. Rev. Fluid Mech.* 46, 255–272.
- Irlandoust, S., Ertlé, S., Andersson, B., 1992. Gas-liquid mass transfer in Taylor flow through a capillary. *Can. J. Chem. Eng.* 70, 115–119.
- Kantarci, N., Borak, F., Ulgen, K.O., 2005. Bubble column reactors. *Process Biochem.* 40, 2263–2283.
- Kjeang, E., Djilali, N., Sinton, D., 2009. Microfluidic fuel cells: A review.

- J. Power Sources 186, 353–369.
- Kloek, W., Van Vliet, T., Meinders, M., 2001. Effect of bulk and interfacial rheological properties on bubble dissolution. *J. Colloid Interface Sci.* 237, 158–166.
- Kuhn, S., Jensen, K.F., 2012. A pH-sensitive laser-induced fluorescence technique to monitor mass transfer in multiphase flows in microfluidic devices. *Ind. Eng. Chem. Res.* 51, 8999–9006.
- Kundu, P.K., Cohen, I.M., Dowling, D.R., 2011. *Fluid Mechanics*, 5th ed. London: Academic.
- Laborie, B., Rouyer, F., Angelescu, D., Lorenceau, E., 2016. On the stability of the production of bubbles in yield-stress fluid using flow-focusing and T-junction devices. *Phys. Fluids* 28, 063103.
- Lefortier, S.G., Hamersma, P.J., Bardow, A., Kreutzer, M.T., 2012. Rapid microfluidic screening of CO₂ solubility and diffusion in pure and mixed solvents. *Lab Chip* 12, 3387–3391.
- Lifton, V.A., 2016. Microfluidics: an enabling screening technology for enhanced oil recovery (EOR). *Lab Chip* 16, 1777–1796.
- Liu, N., Aymonier, C., Lecoutre, C., Garrabos, Y., Marre, S., 2012. Microfluidic approach for studying CO₂ solubility in water and brine using confocal raman spectroscopy. *Chem. Phys. Lett.* 551, 139–143.
- Maalej, S., Benadda, B., Otterbein, M., 2001. Influence of pressure on the hydrodynamics and mass transfer parameters of an agitated bubble reactor. *Chem. Eng. Technol.* 24, 77–84.
- Marre, S., Roig, Y., Aymonier, C., 2012. Supercritical microfluidics: Opportunities in flow-through chemistry and materials science. *J. Supercrit. Fluids* 66, 251–264.
- Meunier, N., Chauvy, R., Mouhoubi, S., Thomas, D., De Weireld, G., 2020. Alternative production of methanol from industrial CO₂. *Renewable Energy* 146, 1192–1203.
- Morais, S., Liu, N., Diouf, A., Bernard, D., Lecoutre, C., Garrabos, Y., Marre, S., 2016. Monitoring CO₂ invasion processes at the pore scale using geological labs on chip. *Lab Chip* 16, 3493–3502.
- Mukherjee, M., Misra, S., 2018. A review of experimental research on enhanced coal bed methane (ECBM) recovery via CO₂ sequestration. *Earth Sci. Rev.* 179, 392–410.
- Nguyen, P., Mohaddes, D., Riordon, J., Fadaei, H., Lele, P., Sinton, D., 2015. Fast fluorescence-based microfluidic method for measuring minimum miscibility pressure of CO₂ in crude oils. *Anal. Chem.* 87, 3160–3164.
- NIST, 2020. NIST standard reference database number 69. URL: <https://webbook.nist.gov/chemistry/>.
- Ogasawara, K., Yamasaki, A., Teng, H., 2001. Mass transfer from CO₂ drops traveling in high-pressure and low-temperature water. *Energy Fuels* 15, 147–150.
- Orr, F.M., et al., 2018. Carbon capture, utilization, and storage: an update. *SPE J.* 23, 2–444.
- Pereira, L.M., Chapoy, A., Burgass, R., Oliveira, M.B., Coutinho, J.A., Tohidi, B., 2016. Study of the impact of high temperatures and pressures on the equilibrium densities and interfacial tension of the carbon dioxide/water system. *J. Chem. Thermodyn.* 93, 404–415.
- Pinho, B., Girardon, S., Bazer-Bachi, F., Bergeot, G., Marre, S., Aymonier, C., 2014. A microfluidic approach for investigating multicomponent system thermodynamics at high pressures and temperatures. *Lab Chip* 14, 3843–3849.
- Pinho, B., Girardon, S., Bazer-Bachi, F., Bergeot, G., Marre, S., Aymonier, C., 2015. Simultaneous measurement of fluids density and viscosity using HP/HT capillary devices. *J. Supercrit. Fluids* 105, 186–192.
- Pohorecki, R., 2007. Effectiveness of interfacial area for mass transfer in two-phase flow in microreactors. *Chem. Eng. Sci.* 62, 6495–6498.
- Prabu, V., Mallick, N., 2015. Coalbed methane with CO₂ sequestration: An emerging clean coal technology in india. *Renewable Sustainable Energy Rev.* 50, 229–244.
- Qin, N., Wen, J.Z., Chen, B., Ren, C.L., 2018. On nonequilibrium shrinkage of supercritical CO₂ droplets in a water-carrier microflow. *Appl. Phys. Lett.* 113, 033703.
- Qin, N., Wen, J.Z., Ren, C.L., 2017. Highly pressurized partially miscible liquid-liquid flow in a micro-T-junction. I. experimental observations. *Phys. Rev. E* 95, 043110.
- Ren, J., He, S., Ye, C., Chen, G., Sun, C., 2012. The ozone mass transfer characteristics and ozonation of pentachlorophenol in a novel microchannel reactor. *Chem. Eng. J.* 210, 374–384.
- Salari, A., Xu, J., Koliou, M.C., Tsai, S.S., 2020. Expansion-mediated breakup of bubbles and droplets in microfluidics. *Phys. Rev. Fluids* 5, 013602.
- Sell, A., Fadaei, H., Kim, M., Sinton, D., 2013. Measurement of CO₂ diffusivity for carbon sequestration: A microfluidic approach for reservoir-specific analysis. *Environ. Sci. Technol.* 47, 71–78.
- Sellami, N., Dewar, M., Stahl, H., Chen, B., 2015. Dynamics of rising CO₂ bubble plumes in the qics field experiment: Part 1—the experiment. *Int. J. Greenhouse Gas Control* 38, 44–51.
- Shah, Y., Kelkar, B.G., Godbole, S., Deckwer, W.D., 1982. Design parameters estimations for bubble column reactors. *AIChE J.* 28, 353–379.
- Sharbatian, A., Abedini, A., Qi, Z., Sinton, D., 2018. Full characterization of CO₂-oil properties on-chip: solubility, diffusivity, extraction pressure, miscibility, and contact angle. *Anal. Chem.* 90, 2461–2467.
- Shim, S., Wan, J., Hilgenfeldt, S., Panchal, P.D., Stone, H.A., 2014. Dissolution without disappearing: Multicomponent gas exchange for CO₂ bubbles in a microfluidic channel. *Lab Chip* 14, 2428–2436.
- Singh, H., 2018. Impact of four different CO₂ injection schemes on extent of reservoir pressure and saturation. *Adv. Geo-Energy Res.* 2, 305–318.
- Sinton, D., 2014. Energy: the microfluidic frontier. *Lab Chip* 14, 3127–3134.
- Sun, R., Cubaud, T., 2011. Dissolution of carbon dioxide bubbles and microfluidic multiphase flows. *Lab Chip* 11, 2924–2928.
- Teng, H., Yamasaki, A., 2000. Dissolution of buoyant CO₂ drops in a counterflow water tunnel simulating the deep ocean waters. *Energy Convers. Manage.* 41, 929–937.
- Teng, Y., Zhang, D., 2018. Long-term viability of carbon sequestration in deep-sea sediments. *Sci. Adv.* 4, eaao6588.
- Tumarkin, E., Nie, Z., Park, J.I., Abolhasani, M., Greener, J., Sherwood-Lollar, B., Günther, A., Kumacheva, E., 2011. Temperature-controlled ‘breathing’ of carbon dioxide bubbles. *Lab Chip* 11, 3545–3550.
- Utada, A.S., Fernandez-Nieves, A., Gordillo, J.M., Weitz, D.A., 2008. Absolute instability of a liquid jet in a coflowing stream. *Phys. Rev. Lett.* 100, 014502.
- Utada, A.S., Fernandez-Nieves, A., Stone, H.A., Weitz, D.A., 2007. Dripping to jetting transitions in coflowing liquid streams. *Phys. Rev. Lett.* 99, 094502.
- Van’t Riet, K., 1979. Review of measuring methods and results in nonviscous gas-liquid mass transfer in stirred vessels. *Ind. Eng. Chem. Process Des. Dev.* 18, 357–364.
- Wilberforce, T., Baroutaji, A., Soudan, B., Al-Alami, A.H., Olabi, A.G., 2019. Outlook of carbon capture technology and challenges. *Sci. Total Environ.* 657, 56–72.
- Wu, H., Cheng, P., 2005. Condensation flow patterns in silicon microchannels. *Int. J. Heat Mass Transfer* 48, 2186–2197.
- Yao, C., Dong, Z., Zhao, Y., Chen, G., 2015. Gas-liquid flow and mass transfer in a microchannel under elevated pressures. *Chem. Eng. Sci.* 123, 137–145.
- Yao, C., Zhao, Y., Ma, H., Liu, Y., Zhao, Q., Chen, G., 2021. Two-phase flow and mass transfer in microchannels: A review from local mechanism to global models. *Chem. Eng. Sci.* 229, 116017.
- Yao, C., Zhu, K., Liu, Y., Liu, H., Jiao, F., Chen, G., 2017. Intensified CO₂ absorption in a microchannel reactor under elevated pressures. *Chem. Eng. J.* 319, 179–190.
- Yue, J., Chen, G., Yuan, Q., Luo, L., Gonthier, Y., 2007. Hydrodynamics and mass transfer characteristics in gas-liquid flow through a rectangular microchannel. *Chem. Eng. Sci.* 62, 2096–2108.
- Yue, J., Luo, L., Gonthier, Y., Chen, G., Yuan, Q., 2009. An experimental study of air-water Taylor flow and mass transfer inside square microchannels. *Chem. Eng. Sci.* 64, 3697–3708.
- Zhang, C., Oostrom, M., Grate, J.W., Wietsma, T.W., Warner, M.G., 2011. Liquid CO₂ displacement of water in a dual-permeability pore network micromodel. *Environ. Sci. Technol.* 45, 7581–7588.
- Zhang, P., Yao, C., Ma, H., Jin, N., Zhang, X., Lü, H., Zhao, Y., 2018. Dynamic changes in gas-liquid mass transfer during Taylor flow in long

- serpentine square microchannels. *Chem. Eng. Sci.* 182, 17–27.
- Zhang, Z., Pan, S.Y., Li, H., Cai, J., Olabi, A.G., Anthony, E.J., Manovic, V., 2020. Recent advances in carbon dioxide utilization. *Renewable Sustainable Energy Rev.* 125, 109799.
- Zhu, P., Kong, T., Lei, L., Tian, X., Kang, Z., Wang, L., 2016. Droplet breakup in expansion-contraction microchannels. *Sci. Rep.* 6, 1–11.